Physics of the Earth and Planetary Interiors 167 (2008) 84–97

Contents lists available at ScienceDirect

Physics of the Earth and Planetary Interiors

journal homepage: www.elsevier.com/locate/pepi

Teleseismic tomography of the upper mantle beneath the southern Lachlan Orogen, Australia

N. Rawlinson*, B.L.N. Kennett

Research School of Earth Sciences, Australian National University, Mills Road, Canberra, ACT 0200, Australia

ARTICLE INFO

Article history:
Received 18 August 2007
Received in revised form 29 January 2008
Accepted 19 February 2008

PACS:
91.30.-f
91.30.Cd
91.30.Jk
91.30.Wx
91.35.Gf

Keywords:
Teleseismic tomography
Non-linear inversion
Southeast Australia
Lachlan Orogen
Lithospheric structure

ABSTRACT

With the goal of better understanding the deep structure and tectonic setting of the Lachlan Orogen, 50 short period seismic stations were deployed across the southern end of the Great Dividing Range in Victoria (southeast Australia) between 2005 and 2006 to record distant earthquakes. A total of 7452 relative P-wave arrival time residuals from 169 teleseismic events have been extracted from the continuous records using an adaptive stacking technique, which exploits the coherency of global phases across the array. These residuals are mapped as three-dimensional perturbations in P-wavespeed in the upper mantle beneath the array using a recently developed iterative non-linear tomographic procedure, which combines a grid based eikonal solver and a subspace inversion technique. The capability of the new scheme to include interface geometry is utilised in order to investigate the effects of *a priori* Moho topography on the resolution of upper mantle structure. The resultant images show a pattern of P-wavespeed anomalies that lacks a predominant orientation, and therefore does not favour a purely W–E subduction–accretion model for the formation of the Lachlan Orogen. One of the main features of the three-dimensional model is a zone of elevated wavespeed beneath the northern end of the array, which extends to a depth of approximately 150 km, and contrasts with significantly lower wavespeeds to the south. This anomaly, which does not appear to be an artifact of relative arrival time residual contributions from the adjoining mountainous terrane, may reflect the presence of a substantial piece of Proterozoic lithosphere incorporated within the Phanerozoic subduction–accretion setting of the Lachlan Orogen. Another key feature of the solution model is a zone of relatively low velocity beneath the newer volcanic province northwest of Melbourne, which extends from the crust to a depth of approximately 200 km. This is likely to represent the signature of elevated temperatures associated with a diffuse mantle source for the Quaternary volcanism in Victoria.

1. Introduction

Prior to the breakup of the Meso-Neoproterozoic supercontinent Rodinia, the Australian land-mass comprised an assemblage of the north, west and south Australian cratons. This amalgamation of Archean and Proterozoic terranes now represents the western two-thirds of the Australian continent, and formed as a result of continent–continent collision, accretion along several subduction fronts, mafic underplating associated with vertical accretion, and several episodes of lithospheric extension (Betts et al., 2002). Distinct blocks of Archean lithosphere contained within this region include the Pilbara and Yilgarn Cratons in Western Australia, and the Gawler Craton in South Australia.

Following the break-up of Rodinia, disassembled elements of the former supercontinent reformed during the Late Neoproterozoic to Early Cambrian to create Gondwana (Meert, 2001). Subsequent convergence along the proto-Pacific margin of east Gondwana formed a series of orogenic belts that date from the Middle Cambrian through to the onset of the break-up of Gondwana and Pangea, at around 227 Ma (Glen, 2005). The Tasman Orogen or "Tasmanides" (Foster and Gray, 2000) comprises the eastern one-third of the present day Australian continent that was accreted along the eastern margin of Precambrian Australia as a result of this process. The Delamerian, Lachlan, New England, Thomson and North Queensland Orogens represent separate components of this Phanerozoic terrane.

In southeast Australia (Fig. 1), the Mid-Late Cambrian Delamerian Orogen, which extends from the mainland into Tasmania (Glen, 2005; Rawlinson et al., 2006a), formed as a result of west-directed subduction along the proto Pacific margin (Betts et al., 2002). The underlying basement consists of Proterozoic lithosphere, which is thought to partially extend beneath the Lachlan Orogen to the

* Corresponding author. Tel.: +61 2 6125 5512; fax: +61 2 6257 2737.
E-mail address: nick@rses.anu.edu.au (N. Rawlinson).
URL: http://rses.anu.edu.au/~nick (N. Rawlinson).

0031-9201/$ – see front matter © 2008 Elsevier B.V. All rights reserved.
doi:10.1016/j.pepi.2008.02.007

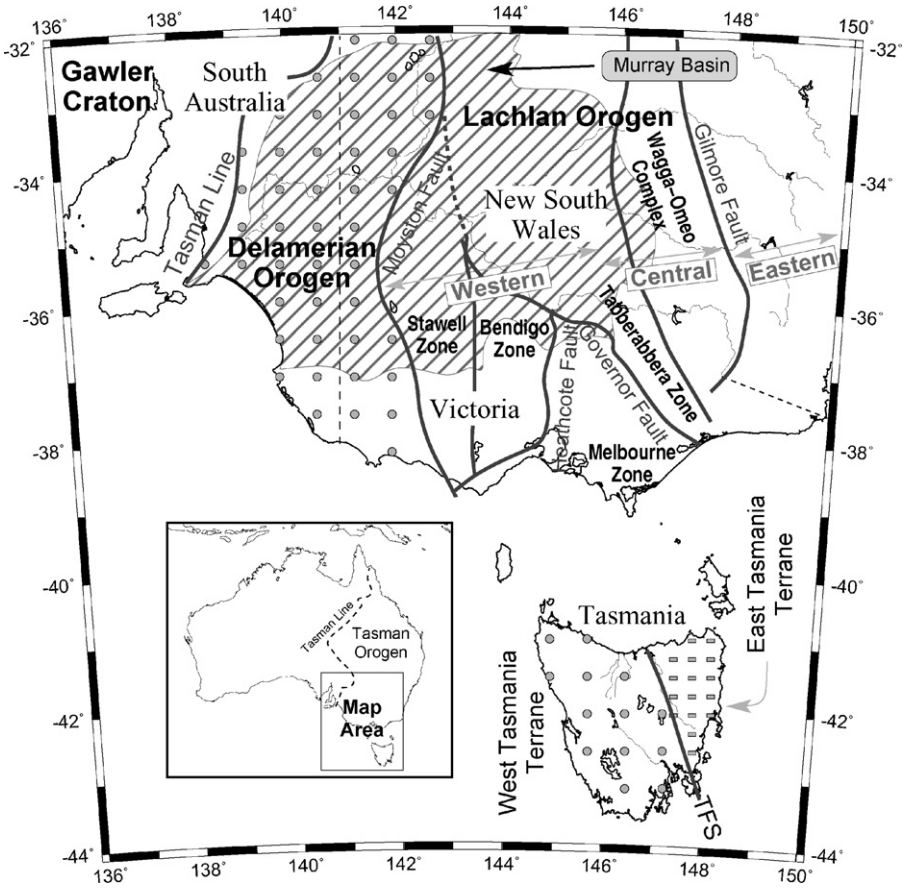

Fig. 1. Schematic map of the southern Tasman Orogen in eastern Australia. The Murray Basin and other Cenozoic deposits obscure much of the underlying Palaeozoic basement. The Murray Basin is denoted by the region of dense parallel lines; the grey dots indicate the presence of Precambrian basement terrane; and the grey rectangles in Tasmania indicate the presence of Palaeozoic basement terrane. TFS: Tamar Fracture System.

east (Glen, 2005; Rawlinson et al., 2006a). The boundary between Phanerozoic eastern Australia and Precambrian western Australia is often represented by a largely inferred "Tasman Line" (Fig. 1); however, recent evidence from potential field data and seismic imaging suggest that the transition is too complex to be represented by a single line (Direen and Crawford, 2003; Kennett et al., 2004).

The tectonic evolution of the Lachlan Orogen (Fig. 1) began in the Late Cambrian, and was largely complete by the Mid-Late Devonian. This is a highly complex region of Australia, the formation of which may have involved multiple subduction zones (Foster and Gray, 2000). However, a solid consensus on this issue remains elusive, with a variety of possible substrates still under consideration, including purely oceanic, mixed oceanic and continental, and continental (Glen, 2005). Correspondingly, tectonic models of the region vary between a predominantly accretionary oceanic system (Foster and Gray, 2000; Fergusson, 2003; Spaggiari et al., 2004) and a largely intracratonic setting (VandenBerg, 1999; Taylor and Cayley, 2000; Willman et al., 2002). It has also been suggested that fragments rifted from the Precambrian craton (Glen, 2005), or "continental ribbons", underlie parts of the Lachlan Orogen within a basement dominated by oceanic crust (Foster and Gray, 2000; Betts et al., 2002). Modern day analogues for the Lachlan Orogeny could potentially range between a Philippine Sea-type marginal ocean basin and a Japan Sea-type backarc basin, although the more complex multiple subduction models (e.g. Foster and Gray, 2000; Fergusson, 2003) that have been proposed in recent times have less obvious associations. Gray and Foster (2004) regard the Lachlan Orogeny as being clearly distinct from the more recent orogenies that produced the Alps, Canadian Rockies and Appalachians.

Previous passive imaging studies of the Australian lithosphere have concentrated on broad variations in shear wavespeed derived from continental scale surface wave tomography. The Australia-wide SKIPPY project (1993–1998) used a rolling array of broadband seismometers to occupy a total of 65 sites with a nominal station spacing of 400 km. Surface wave data from SKIPPY and subsequent deployments have allowed three-dimensional images of shear wavespeed (and azimuthal anisotropy) to be constructed for the entire continent with a horizontal resolution of 200–250 km (Zielhuis and van der Hilst, 1996; Debayle and Kennett, 2003; Simons et al., 2002; Debayle and Kennett, 2003; Fishwick et al., 2005). One clear observation that can be made from all of these studies is that high-shear wavespeeds exist beneath Precambrian western Australia, which contrast with the low wavespeeds beneath Phanerozoic eastern Australia. While there is little evidence for the presence of Proterozoic fragments of continental lithosphere underpinning parts of eastern Australia, the limited lateral resolution of regional surface wave tomography means that such structures are unlikely to be imaged. Higher resolution body wave travel time studies are therefore well placed to address this outstanding issue.

Over the last decade, the emphasis has moved from continental scale imaging to higher density, more localised seismic arrays deployed to target regions of particular geological interest using teleseismic body wave tomography. Studies that have been published to date are LF98 in western Victoria (Graeber et al., 2002), TIGGER in northern Tasmania (Rawlinson et al., 2006b; Rawlinson and Urvoy, 2006) and SEAL in southern NSW (Rawlinson et al., 2006a). Results from the mainland experiments reveal a number

of prominent features in the upper mantle, including pronounced negative velocity anomalies in the vicinity of the recent newer volcanic province (NVP) in western Victoria; elevated wavespeeds associated with the Delamerian Orogen extending beneath the Stawell Zone; and elevated wavespeeds beneath the Wagga–Omeo Complex in New South Wales. In the former case, it is thought that the recent volcanism in Victoria is fuelled by a hot spot which is gradually moving south relative to the contemporary motion of the Australian plate (Paul et al., 2005). One of the main results from the TIGGER experiment, which used station spacings of only 15 km, was that crustal velocities beneath Proterozoic western Tasmania are much higher than those beneath Palaeozoic eastern Tasmania. The transition zone also occurs some 30–50 km east of the Tamar fracture System (Fig. 1), which has traditionally been used to mark the boundary between the two terranes (Williams, 1989).

In this paper, results from the eastern Victoria array (EVA) experiment are published for the first time. EVA involved the deployment of 50 seismic stations across the southern end of the Great Dividing Range (see Fig. 2a) for a period of approximately 8 months. All seismometers are passive vertical component short periods (eigenfrequency of 1 Hz), and connect to internally powered solid state recorders. The use of teleseisms to constrain structure means that the depth interval over which good crossing path coverage can occur is approximately constrained by the station spacing and two-thirds the array aperture (Evans and Achauer, 1993). Thus, the upper mantle between ~45 and 300 km depth has the potential to be well resolved by the EVA dataset.

The placement of the EVA array allows structure beneath the inferred crustal elements between the Bendigo Zone and the Wagga–Omeo Complex (Fig. 1) to be illuminated. Fundamental questions that can be addressed by this study include: (1) is there evidence of Proterozoic crustal fragments or ribbons beneath the Mesozoic and Cenozoic sedimentary and volcanic cover sequences that obscure much of this region?; (2) can the low-velocity anomaly associated with the newer volcanic provinces, observed in the study of Graeber et al. (2002), also be observed beneath the western edge of the EVA array?; (3) does the zone of relatively high velocity beneath the Wagga–Omeo Complex imaged by the SEAL experiment, extend into northern Victoria, and what does it represent?; and (4) is there any evidence of Proterozoic lithosphere from western Tasmania extending northwards beneath Victoria, and if so, of a northward continuation of the so-called Tamar fracture System?

A new tomographic inversion package, called FMTOMO (Fast Marching TOMOgraphy), is used to map relative arrival times from distant events as three-dimensional perturbations in P-wavespeed. A grid-based eikonal solver known as the fast marching method (FMM) is used to solve the forward problem of travel time prediction (de Kool et al., 2006), and a subspace inversion scheme (Kennett et al., 1988) is used to solve the inverse problem of adjusting model parameters to satisfy the data observations. The forward and inverse schemes are applied iteratively to address the non-linearity of the inverse problem. Although FMTOMO has the flexibility to incorporate many different classes of body wave travel time datasets, the paucity of active source experiments and local seismicity in eastern Victoria means that only teleseismic arrivals from EVA are considered in this study. The capability of FMTOMO to include interface structure is used to investigate the effects of variable Moho depth beneath the Great Dividing Range, and its possible influence on the recovery of wavespeed structure in the upper mantle.

2. Data and adaptive stacking

A total of 169 distant earthquake records from the EVA array are used for the extraction of relative arrival time residual maps. All events of magnitude Mw > 6.0 were examined, but within a distance range of ~100°, this threshold was decreased to Mw > 5.0. For events from the south and west, an even lower threshold of Mw > 4.5 was used to ensure optimum azimuthal coverage. The location of Victoria relative to surrounding seismogenic zones means that most of the detected earthquakes originate from convergent plate boundaries to the north and east of the array (Fig. 2b), with relatively few occurring to the south and west, where the margins of the Australian plate are in divergent settings.

First-arriving P-wavetrains from three distant earthquakes recorded by the EVA array are shown in Fig. 3. All traces have been subject to preliminary alignment using travel time predictions from the *ak*135 global reference model (Kennett et al., 1995) for the direct P-phase. Extraction of relative arrival time residual information is achieved using an adaptive stacking technique developed by Rawlinson and Kennett (2004), which exploits the coherency (clearly evident in Fig. 3) of the arriving waveforms across the array.

Previous studies have shown the adaptive stacking technique to be highly robust in the presence of significant data noise and imperfect coherence of waveforms across the array (Rawlinson and

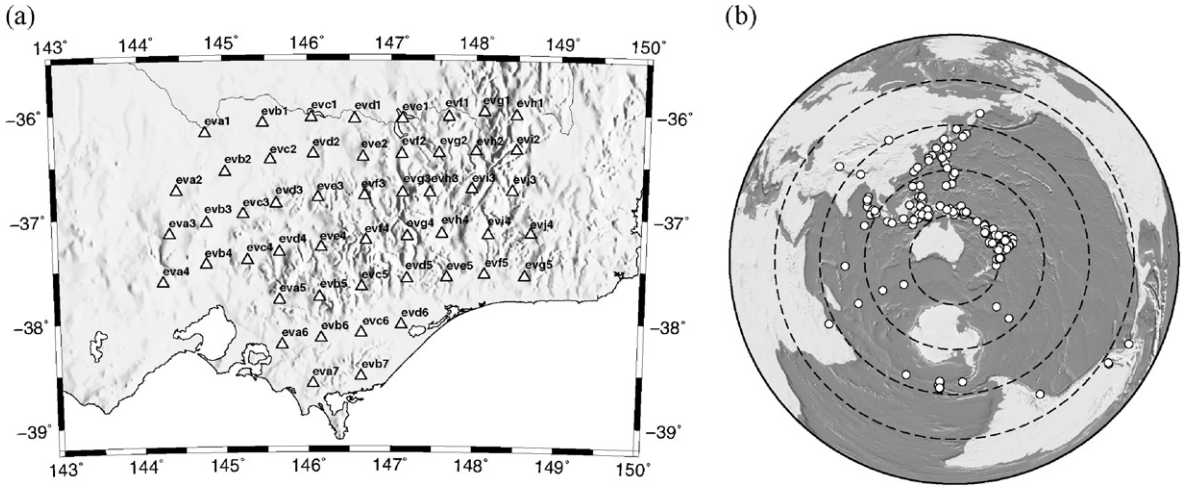

Fig. 2. (a) Location of the 50 EVA stations (open triangles) used in this study. Sites vary in elevation between 9 m (evd6) and 1724 m (evh1); (b) distribution of the 169 teleseismic events (open circles) used in the tomographic inversion for three-dimensional seismic structure beneath eastern Victoria. Dashed circles represent 30° increments in the great circle distance from the centre of the EVA array.

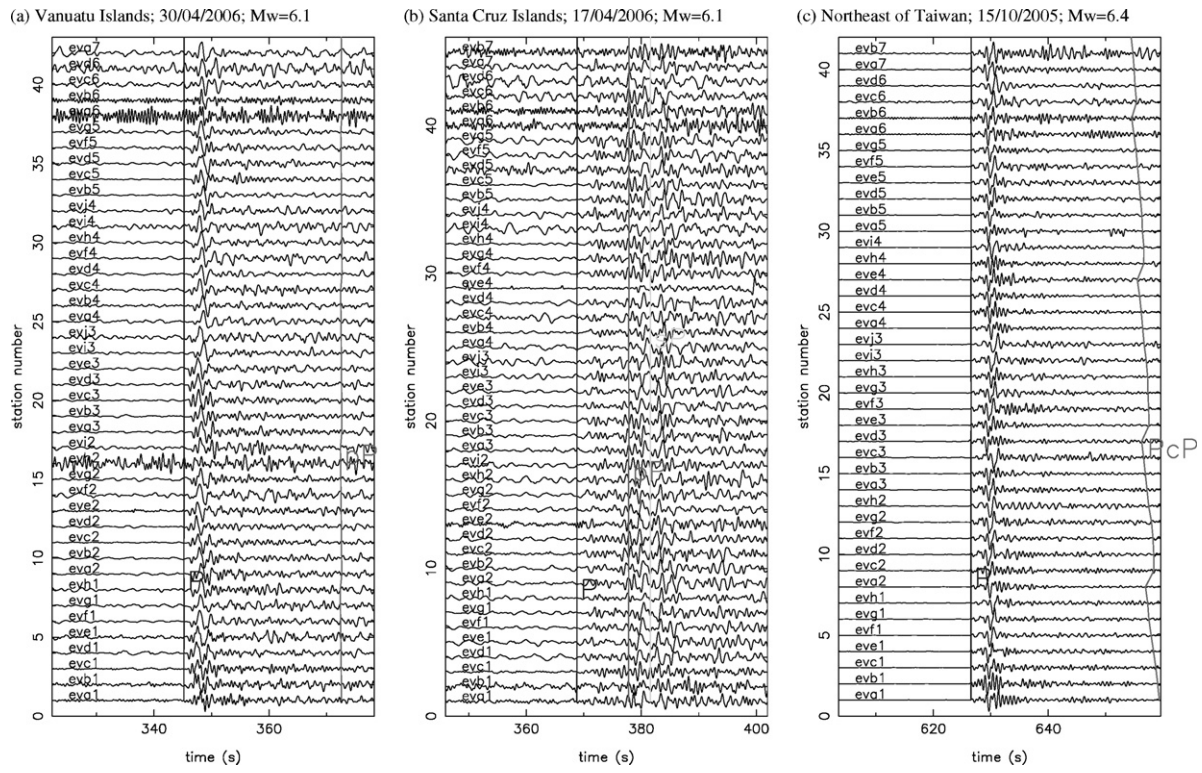

Fig. 3. Records from the EVA array for three different teleseismic events. Trace moveout has been corrected for using the *ak* 135 global reference model. Thick vertical lines show *ak* 135 travel time predictions for several P phases. Note that traces from stations which either did not record data or were extremely noisy are not displayed. (a) Vanuatu Islands event located at 15.1°S, 167.4° E and 128 km depth; (b) Santa Cruz Islands event located at 12.5°S, 166.5° E and 16 km depth; (c) northeast of Taiwan event located at 25.3°N, 123.4° E and 123 km depth.

Kennett, 2004; Rawlinson et al., 2006a, b). An additional benefit of the technique is that uncertainty estimates are automatically produced during the alignment process. These estimates can be used to weight the relative importance of each residual in the tomographic inversion. In this study, a 3 Hz low-pass filter is applied to the data prior to trace alignment; however, as noted in Rawlinson and Kennett (2004), adaptive stacking is relatively tolerant of high-frequency noise.

Relative arrival time residual maps obtained by applying the adaptive stacking process to the three events in Fig. 3 are shown in Fig. 4. Despite the waveforms from the Vanuatu Islands (Fig. 3a) and Santa Cruz Islands (Fig. 3b) being markedly different, and the obvious presence of noise in many traces (particularly Fig. 3b), the adaptive stacking process yields almost identical patterns of relative arrival time residuals. This represents a good validation of the technique, given that the two events are almost co-located. Ostensibly, Fig. 4a and b suggest that the lithosphere beneath the northwest of the array is faster than the lithosphere beneath the south and east of the array. However, relative arrival time residuals are a path integral quantity, with a strong dependence on azimuth and inclination, so careful analysis is required in order to make meaningful structural inferences from these type of maps. Indeed, the residual patterns yielded by these two events are very different to that of Fig. 4c, which corresponds to the P arrival from an earthquake to the northeast of Taiwan. From the 169 earthquakes used in this study, a total of 181 coherent phases were targeted for adaptive stacking. For the most part, these were direct P (as in Fig. 4), but also included a total of 30 pP, sP, ScP, PcP, PKiKP and PP phases. The availability of other phases with different incidence angles has a beneficial effect on the tomographic imaging. In total, 7452 relative arrival time residuals were extracted.

3. Method

Teleseismic tomography is used to map the patterns of relative arrival time residuals obtained in the previous section as three-dimensional perturbations in P-wavespeed from a depth dependent reference model. One of the principal assumptions of this technique is that relative arrival time residual patterns are largely unaffected by lateral variations in structure outside a local model volume defined beneath the array (Aki et al., 1977; Oncescu et al., 1984; Humphreys and Clayton, 1990; Achauer, 1994; Steck et al., 1998; Graeber et al., 2002; Rawlinson et al., 2006b). Here, a new tomographic inversion package called FMTOMO is used to perform the teleseismic tomography.

The origins of FMTOMO go back to the work of Rawlinson and Sambridge (2004a, b, 2005), who developed a robust and efficient scheme for tracking phases comprising multiple reflection and refraction branches in complex two-dimensional Cartesian media. A grid based eikonal solver known as the Fast Marching Method or FMM (Sethian, 1996, 2001; Popovici and Sethian, 2002) is used to track the propagating wavefront through a gridded velocity field. FMM achieves its robustness by solving the eikonal equation using upwind entropy satisfying operators, and computational efficiency by tracking the first-arrival wavefront along a narrow band of grid points. Rawlinson and Sambridge (2004a, b) extended the method to allow interfaces to be included by locally suturing interface nodes to neighbouring velocity nodes with an irregular triangulation. In order to track refraction and reflection branches, FMM is re-initialised from the travel time surface along the interface into either adjoining layer. In theory, phases comprising any number of refraction and reflection branches can be tracked.

The multi-stage FMM scheme was extended to three-dimensional spherical coordinates by de Kool et al. (2006), who

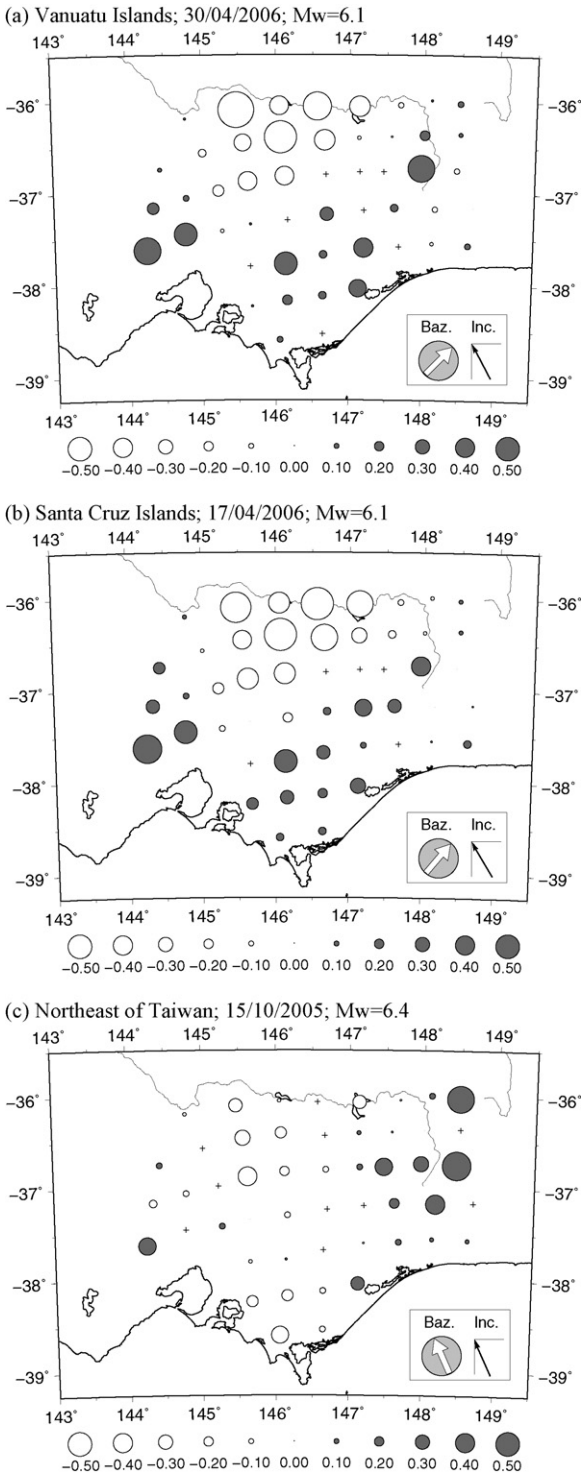

Fig. 4. Relative arrival time residual maps (in seconds) obtained by aligning traces from each of the three events shown in Fig. 3 with the adaptive stacking technique of Rawlinson and Kennett (2004). Stations which did not record usable data are denoted with a cross. Baz. denotes event back-azimuth; Inc. denotes path inclination at receiver array.

added greater flexibility by allowing teleseismic phases to be included. This is achieved by computing travel times from a distant source through a global reference model (e.g. *ak*135) to the boundary nodes of a given three-dimensional model volume. FMM is then initialised by using the boundary node travel times as the starting narrow band of points for the subsequent wavefront tracking. Compared to conventional ray tracing schemes (e.g. Julian and Gubbins, 1977; Um and Thurber, 1987; Prothero et al., 1988; Sambridge, 1990; Bulant, 1996; Rawlinson et al., 2001) the multi-stage FMM has several potential advantages, including stability (it is capable of always converging to the correct high frequency solution as grid spacing is reduced), always locating the first-arrival of any specified phase, and computational efficiency (particularly when there are many more sources than receivers or vice versa).

FMTOMO uses the multi-stage FMM of de Kool et al. (2006) to solve the forward problem of travel time prediction. Model structure is represented by subhorizontal layers of variable thickness. Wavespeed within each layer is defined by an independent grid of velocity nodes, with cubic B-spline functions (Bartels et al., 1987) used to create a smoothly varying, locally controlled velocity continuum. Similarly, each interface is defined by a grid of interface depth nodes, with cubic B-splines used to create a smoothly varying, locally controlled surface. Although layers and interfaces horizontally span the model region, interfaces can merge to create layer pinchouts if required.

The goal of the FMTOMO package is to allow any combination of source location, velocity and interface structure to be inverted for using most classes of travel time dataset, including reflection, wide-angle reflection and refraction, local earthquake, regional and teleseismic. The inverse problem of adjusting model parameter values to satisfy the data observations is solved using an iterative non-linear approach, which equates to the gradient-based minimisation of the following objective function:

$$S(\mathbf{m}) = (\mathbf{g}(\mathbf{m}) - \mathbf{d}_{\text{obs}})^{\text{T}}\mathbf{C}_{\text{d}}^{-1}(\mathbf{g}(\mathbf{m}) - \mathbf{d}_{\text{obs}}) + \epsilon(\mathbf{m} - \mathbf{m}_0)^{\text{T}}\mathbf{C}_{\text{m}}^{-1}(\mathbf{m} - \mathbf{m}_0) + \eta\mathbf{m}^{\text{T}}\mathbf{D}^{\text{T}}\mathbf{D}\mathbf{m} \quad (1)$$

where $\mathbf{m}$ are the model parameters, $\mathbf{d}_{\text{obs}}$ the observed residuals, $\mathbf{g}(\mathbf{m})$ the predicted residuals, $\mathbf{C}_{\text{d}}$ the *a priori* data covariance matrix, $\mathbf{C}_{\text{m}}$ the *a priori* model covariance matrix, and $\mathbf{D}$ is a second derivative smoothing operator. The level of imposed regularisation is controlled by the damping parameter ϵ and the smoothing parameter η, which govern the trade-off between how well the solution satisfies the data, the proximity of the solution model to the reference model, and the smoothness of the solution model.

The objective function is minimised by successively updating some given initial model using a subspace inversion scheme (Kennett et al., 1988), which requires that $S(\mathbf{m})$ is locally linearisable. Thus for some current model $\mathbf{m}_i$, a new model $\mathbf{m}_{i+1} = \mathbf{m}_i + \delta\mathbf{m}_i$ is produced where the model perturbation $\delta\mathbf{m}_i$ is supplied by the subspace inversion method. After each iteration, the multistage FMM is applied to update path and travel time information. The scheme progresses until the observed data are satisfied or the model perturbations $\delta\mathbf{m}_i$ converge to zero. The subspace inversion scheme operates by projecting the quadratic approximation of $S(\mathbf{m})$ on to an n-dimensional subspace of model space. For the objective function defined by Eq. (1), the subspace model perturbation is given by (see Rawlinson and Sambridge, 2003, for a derivation):

$$\delta\mathbf{m} = -\mathbf{A}[\mathbf{A}^{\text{T}}(\mathbf{G}^{\text{T}}\mathbf{C}_{\text{d}}^{-1}\mathbf{G} + \epsilon\mathbf{C}_{\text{m}}^{-1} + \eta\mathbf{D}^{\text{T}}\mathbf{D})\mathbf{A}]^{-1}\mathbf{A}^{\text{T}}\hat{\boldsymbol{\gamma}} \quad (2)$$

where $\mathbf{A} = [\mathbf{a}^j]$ is an $M \times n$ projection matrix (for M unknowns), $\mathbf{a}^j$ $(j = 1, \ldots, n)$ the component direction vectors, $\mathbf{G}$ the matrix of Fréchet derivatives and $\hat{\boldsymbol{\gamma}}$ is the gradient vector ($\hat{\boldsymbol{\gamma}} = \partial S/\partial\mathbf{m}$). The basis vectors that span the n-dimensional subspace are here based on the gradient vector in model space, and its pre-multiplication by the model space Hessian (see Kennett et al., 1988; Rawlinson and Sambridge, 2003, for more details). The subspace method has several desirable characteristics, including low-computational cost for large inverse problems, and naturally dealing with different parameter classes (e.g. velocity, interface depth, source location). Only a

relatively small $n \times n$ matrix needs to be inverted in order to compute $\delta\mathbf{m}$—e.g., Williamson (1990) uses $n = 6$, and Rawlinson et al. (2006b) uses $n = 10$. The basis vectors $[\mathbf{a}^j]$ that form the projection matrix **A** are chosen such that each orthogonal vector lies in the space spanned by only one parameter class. For large n, **A** may not completely span all n dimensions, in which case singular value decomposition (SVD) is used to identify and remove unnecessary basis vectors.

4. Results

4.1. Tomographic solution model

FMTOMO is used to invert the 7452 relative arrival time residuals extracted from the EVA dataset for variations in P-wavespeed beneath eastern Victoria. A total of 74,664 velocity nodes spaced approximately 20 km apart in latitude, longitude and depth are used to define the model. The laterally invariant reference or starting model is based on one-dimensional velocity vs. depth curves obtained from a refraction study of the Lachlan Orogen (Collins, 1991). However, since these curves only extend into the uppermost mantle, *ak*135 velocity values are used to define velocities below approximately 50 km depth. The complete inversion procedure is carried out using six iterations of a 20-dimensional subspace inversion scheme with $\epsilon = 5$ and $\eta = 10$. The damping and smoothing values are chosen using the approach of Rawlinson et al. (2006b), which is based on a three step procedure using trade-off curves between data variance and model roughness, and data variance and model variance.

In addition to velocity grid node values, station terms are also included as unknowns in the inversion. These terms, of which there are 50 (one per station), have units of time, and are used to absorb the relative arrival time residual contribution from unconstrained crustal structure, which otherwise would be mapped as spurious velocity perturbations along the ray paths [the effectiveness of this approach is examined more closely in Section 4.3]. Due to the way that they were picked, the observed relative arrival time residuals contain a contribution from structural variations, and a contribution from variations in elevation. The latter component is accounted for by ensuring that the stations are at their correct elevations in the inversion model.

The final solution model reduces the data variance from 0.072 to 0.011 s^2, a reduction of 85%. This corresponds to an RMS reduction from 269 to 104 ms. The data variance reduction due to structure alone (excluding contributions from elevation) is 80%. The estimated standard deviation of the data noise is 68 ms, which means that the solution model fits the data to an acceptable level. The remaining misfit can be attributed to unresolved variations in crustal structure, which can be short wavelength and high amplitude, deep mantle structure beneath the local model volume, and anisotropy. Of course, the intrinsic regularisation imposed by the choice of parameterisation may also limit the ability of the solution model to satisfy the data. Fig. 5 shows a frequency histogram of the relative arrival time residuals for the initial and solution models.

A series of horizontal and vertical slices through the P-wavespeed solution model are shown in Figs. 6 and 7, respectively. At shallow depths (e.g. Fig. 6a and b), the pattern of anomalies is dominated by positive wavespeed perturbations to the northwest, and negative perturbations to the southeast, which are broadly consistent with the relative arrival time residual patterns observed in Fig. 4. The maximum perturbations at 50 km depth are of the order ±3.8%, and in general these perturbations tend to decrease with increasing depth. The E–W (Fig. 7a) and N–S (Fig. 7b) cross-sections also reflect the presence of elevated wavespeeds in the northwest sector of the model. At greater depths (Fig. 6e and f), the pattern of anomalies changes to one that features a fast anomaly centred beneath the array. Visible evidence of structural smearing along dominant ray path orientations can be observed in Fig. 7b(i) and b(ii) in particular, although as these cross-sections lie beneath the western edge of the array, which has a smaller N–S span, this is relatively unsurprising.

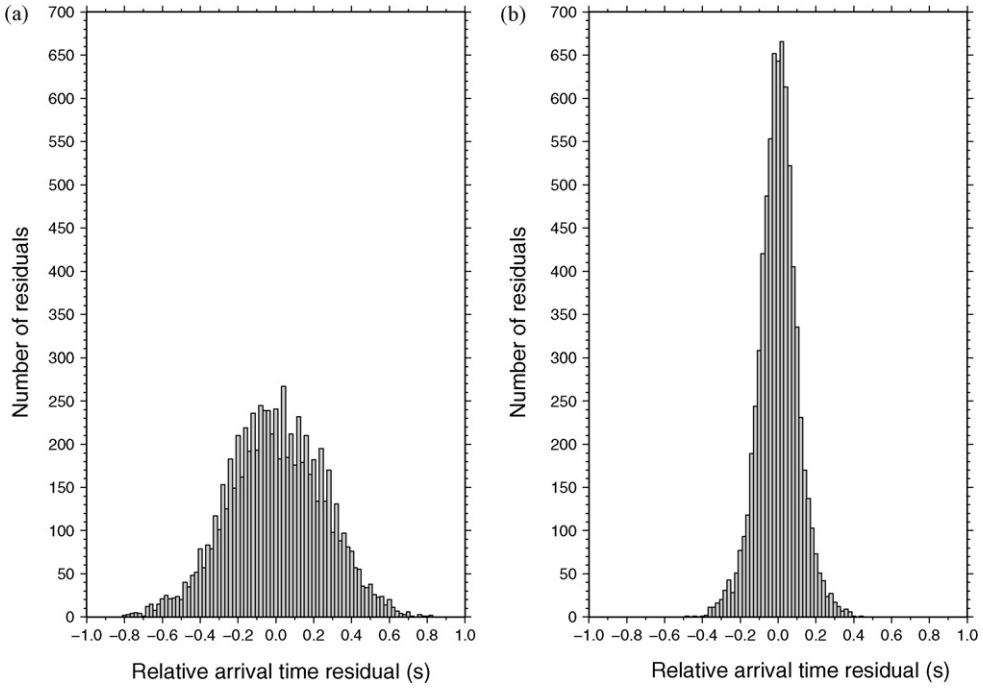

Fig. 5. Frequency histograms showing the magnitude and distribution of relative arrival time residuals associated with the initial model (a) and solution model (b).

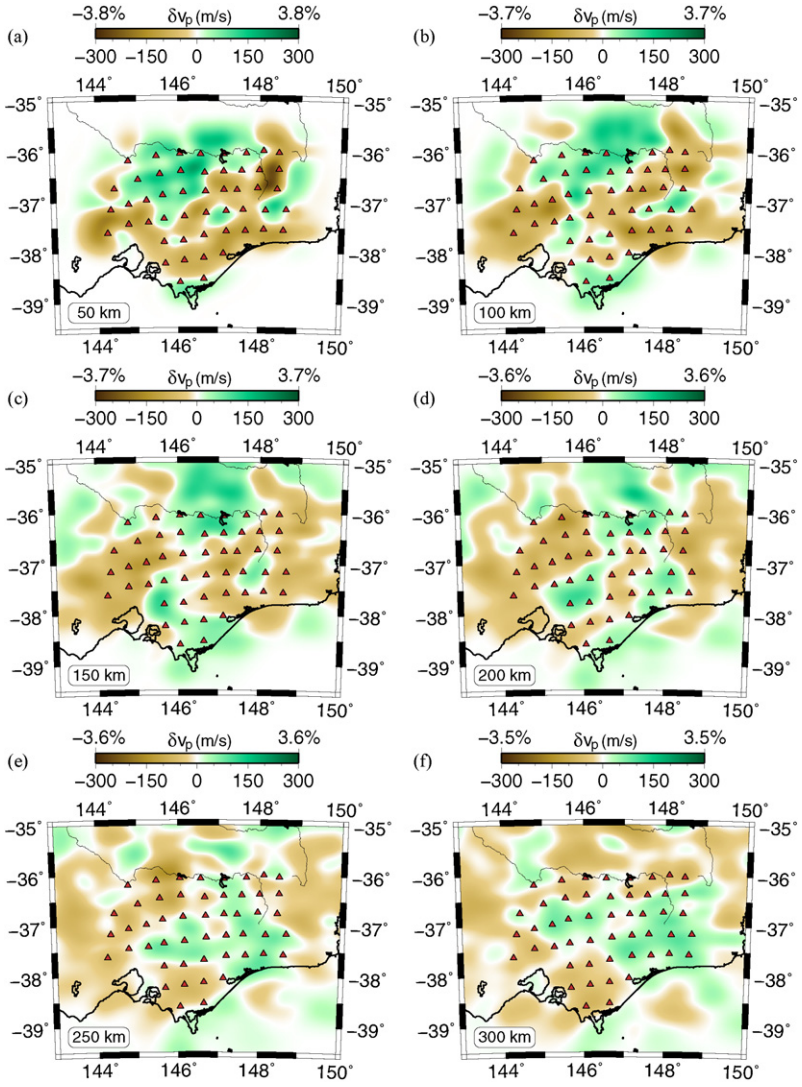

Fig. 6. Horizontal sections through the three-dimensional solution model obtained by inversion of EVA relative arrival time residual data. P-wavespeed perturbations from a reference one-dimensional model are represented using colour contouring. (For interpretation of the references to colour information in this figure legend, the reader is referred to the web version of the article.)

The station terms obtained from the inversion of EVA relative arrival time residuals are shown in Fig. 8, together with station elevations. If variations in crustal thickness were the dominant shallow structural variation above 50 km depth (approximately where ray paths cease to cross), then one might expect to see the pattern of station terms correlate with changes in elevation, i.e., large positive terms associated with significant elevation. As Fig. 8 shows, no such correlation is apparent, a result which has several possible explanations: (1) lateral wavespeed anomalies in the crust contribute to the relative arrival time residual patterns at least to the same degree as variations in crustal thickness; (2) the lithospheric strength is such that thick crustal roots do not underlie the mountainous regions; (3) the trade-off between station terms and shallow velocity perturbations cannot be adequately resolved. With regard to the trade-off issue, the broad-scale variations in wavespeed seen in the 50 km depth slice (Fig. 6a) share some similarity with the surface topography, i.e., negative anomalies have a tendency to underlie the elevated regions. Further investigation to assess the potential for crustal anomalies to be smeared into upper mantle structure is therefore warranted prior to interpretation of the three-dimensional model.

4.2. Resolution tests

In this section, the extent to which model parameters are constrained by the EVA arrival time dataset is investigated via a series of synthetic resolution tests. This makes it possible to evaluate which features of the solution model are required to explain the data and which are not. Factors that contribute to solution non-uniqueness include inadequate angular path coverage (i.e. a lack of crossing rays) and arrival time uncertainty.

The first synthetic resolution test that is undertaken here is the so-called "checkerboard test" (Hearn and Clayton, 1986; Glahn and Granet, 1993; Graeber and Asch, 1999; Rawlinson and Sambridge, 2003), which involves the construction of a model consisting of an alternating pattern of fast and slow anomalies. A synthetic dataset is then created by solving the forward problem of travel time prediction using the same source–receiver configuration and phase types as the observational dataset. Application of the tomographic inversion scheme to this dataset will recover the checkerboard pattern in well resolved regions of the model. The checkerboard model used in this case is shown in Fig. 9 (left column). Note that the pattern varies in latitude, longitude and depth. In order to simulate the

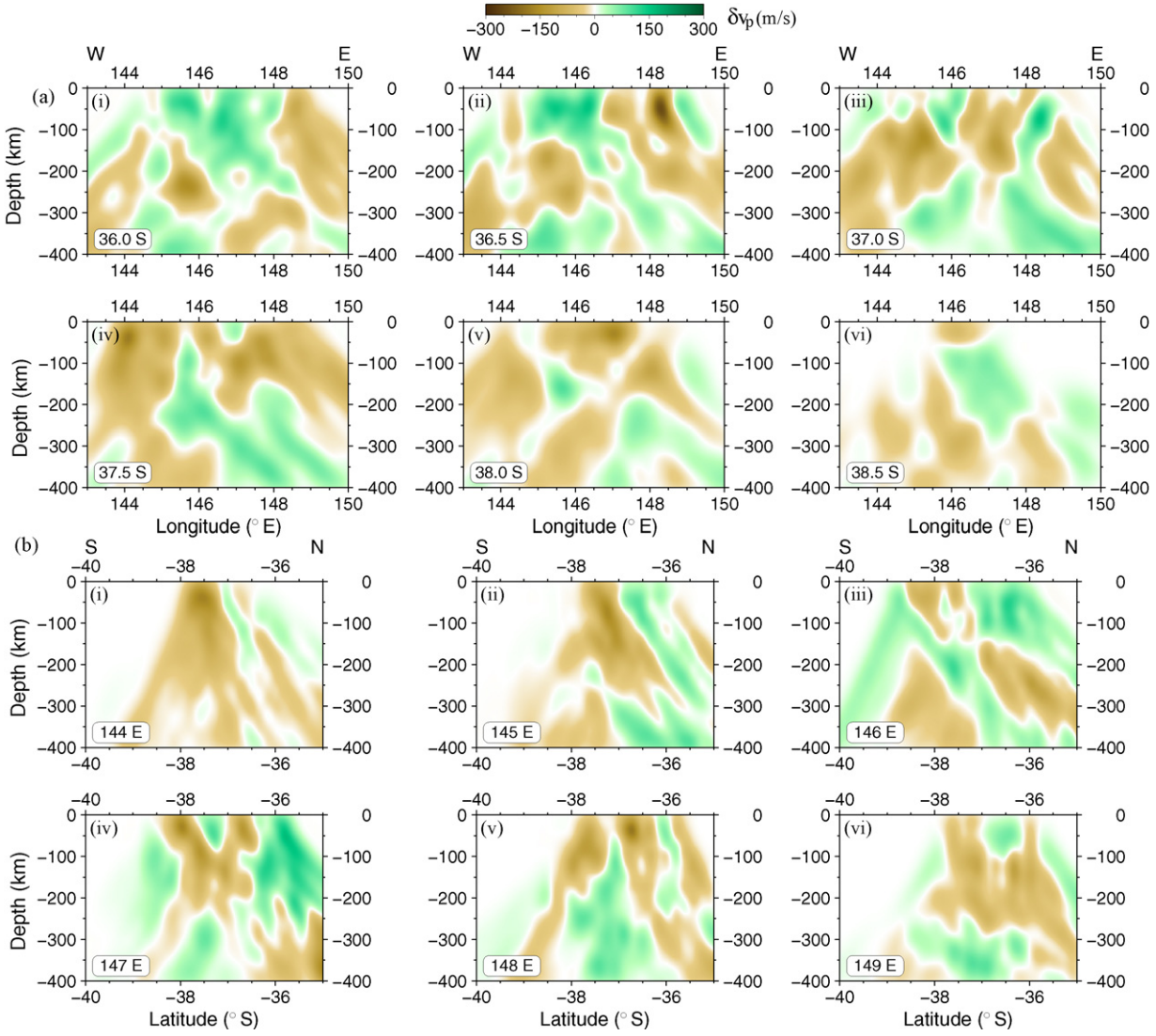

Fig. 7. Vertical slices through the three-dimensional solution model obtained by inversion of EVA relative arrival time residual data. (a) E–W cross-sections; (b) N–S cross-sections.

presence of data noise, Gaussian noise with a standard deviation of 68 ms, which is equal to the estimate for the observational dataset made by the adaptive stacking process, is added to the synthetic residuals. An alternating pattern of station terms with an amplitude of 150 ms (Fig. 10a) is also added to the synthetic dataset to reflect the presence of unresolved shallow structure.

The results of the inversion of the synthetic dataset for both P-wavespeed and station term anomalies are shown in Fig. 9 (centre and right columns) and Fig. 10b, respectively. Although smearing is clearly present in some regions of the velocity model (e.g. Fig. 9b(iii)), the overall recovery of the basic checkerboard pattern is generally good. One expected feature of the solution model is that wavespeed anomalies are lower in amplitude compared to the input model; this occurs largely as a result of the smoothing and damping regularisation that is imposed. As shown in Fig. 2b, most earthquakes used in this study originate from collision zones to the north and east of the array. The consequences of this variable distribution in source azimuth can be observed in Fig. 9c, which shows a tendency to elongate structure in a northerly direction at a dip angle of approximately 45°. A lack of paths from the south gives rise to the increased region of smearing that is present in the E–W slice at 37.5° S (Fig. 9b(iii)) compared to the E–W slice at 36.0° S (Fig. 9b(ii)).

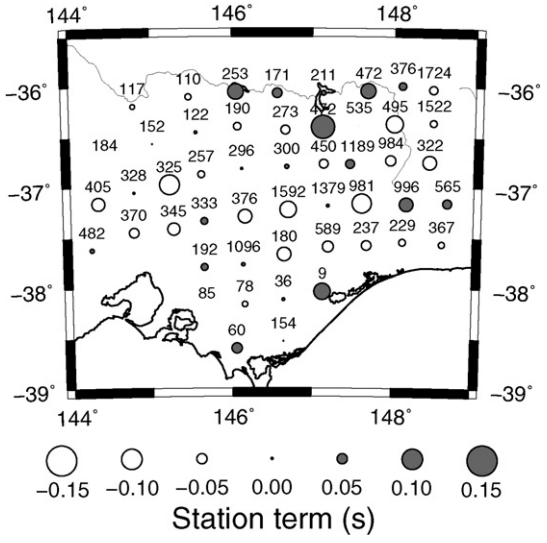

Fig. 8. Station terms obtained from the inversion of EVA relative arrival time residual data. The label above each term indicates station elevation in meters. Positive station terms imply the presence of shallow low-velocity anomalies; negative station terms imply the presence of shallow high-velocity anomalies.

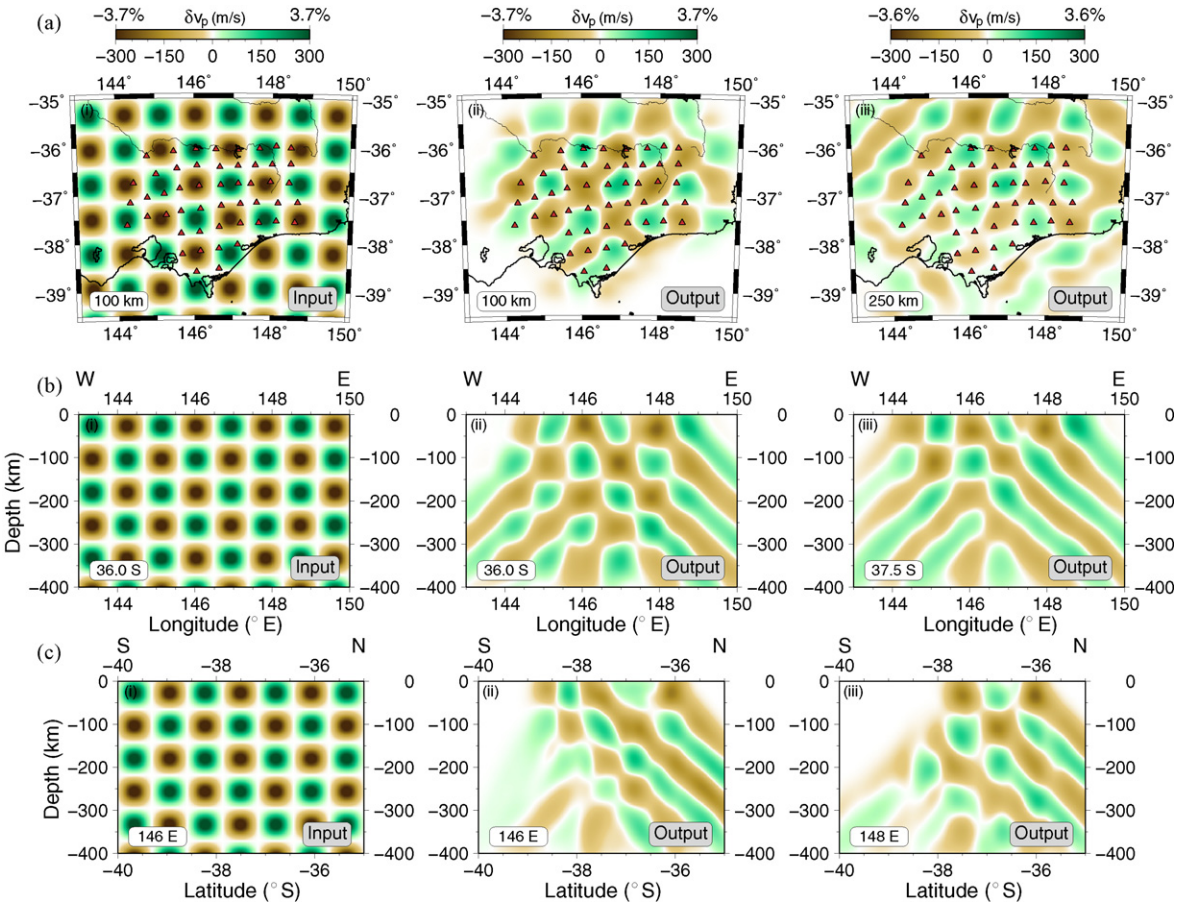

Fig. 9. Checkerboard resolution test results. (a) Horizontal slices; (b) E–W cross-sections; (c) N–S cross-sections. The left hand column shows the synthetic (or input) checkerboard model, and the centre and right hand columns show the recovered (or output) model at different locations.

Overall, this test appears to indicate that structure within the horizontal bounds of the array, to a depth of approximately 300 km, is generally well resolved by the data.

The recovery of the pattern of station term anomalies (Fig. 10), which is done jointly with the velocity anomalies, is largely successful, although there is some variability in the amplitude of the station terms. This is to be expected, because there will always be some trade-off between the station terms and the velocity model; intrinsically the data are not capable of uniquely constraining both of these parameter classes. However, if station terms are not included in the inversion, then the recovery of the synthetic velocity model is less successful, which demonstrates that in cases where shallow structure is poorly constrained by data, the use of station terms can yield positive results. The station terms recovered from the inversion of the EVA dataset are well below 100 ms in most cases (see Fig. 8), and therefore do not have a strong influence on the pattern of recovered velocity anomalies, i.e., performing an inversion without station terms yields a velocity model that is not significantly different. This would indicate that there are no shallow high-amplitude anomalies beneath any of the stations, but it should be noted that

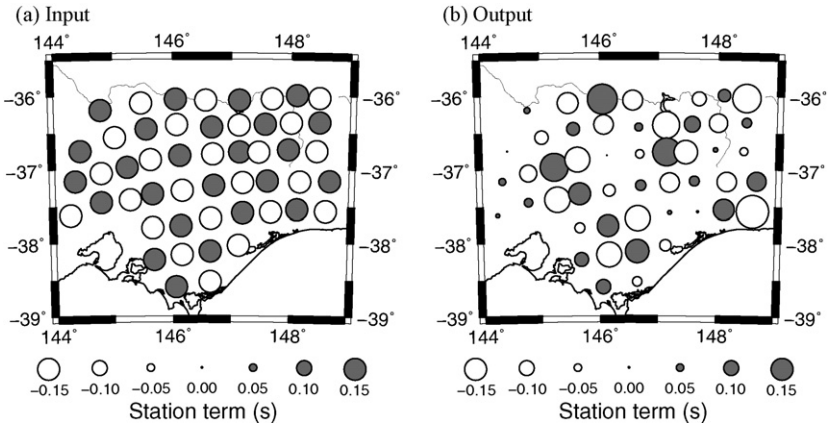

Fig. 10. Checkerboard resolution test results for the station terms. (a) Synthetic station terms (input); (b) recovered station terms (output). Note that these terms were inverted for jointly with the P-wavespeed checkerboard shown in Fig. 9.

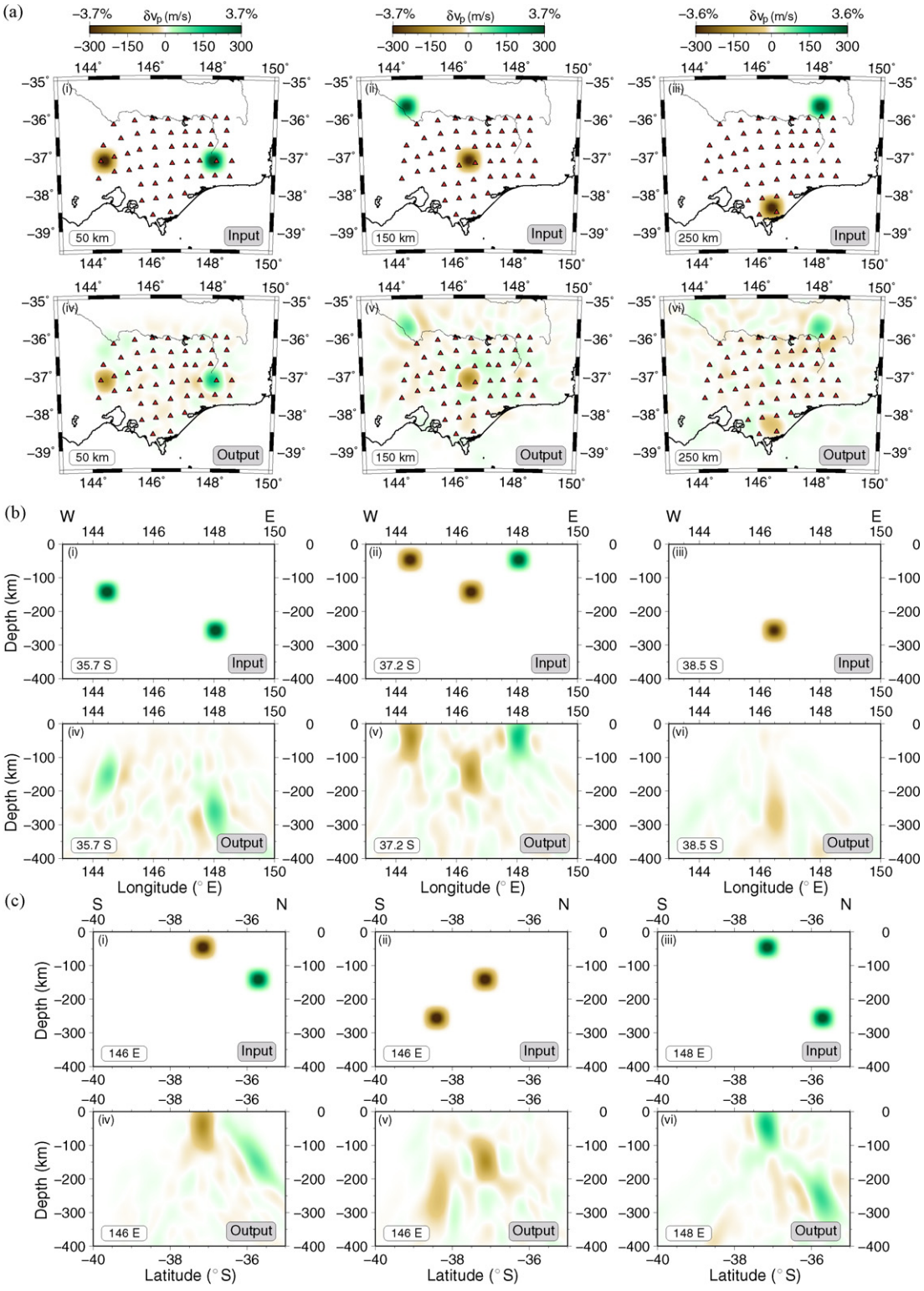

Fig. 11. Synthetic test results showing the recovery of six discrete anomalies. (a) Depth slices; (b) E–W cross-section; (c) N–S cross-sections.

the potential for trade-off between travel time and velocity still exists.

One drawback of using a checkerboard test to assess the resolving power of teleseismic data is that when anomalies are smeared out along predominant ray trajectories, they tend to merge with diagonally adjacent anomalies of the same sign. Moreover, the gradient of the checkerboard pattern continuously fluctuates, which adds to the difficulty of evaluating the actual distortion of recovered structure. Therefore, another synthetic test involving the attempted recovery of six spatially separated short wavelength anomalies is carried out. As before, Gaussian noise is added to the synthetic relative arrival time residuals to replicate the uncertainty associated with the observations. Fig. 11 shows a series of cross-sections through the synthetic and recovered models. All of the output

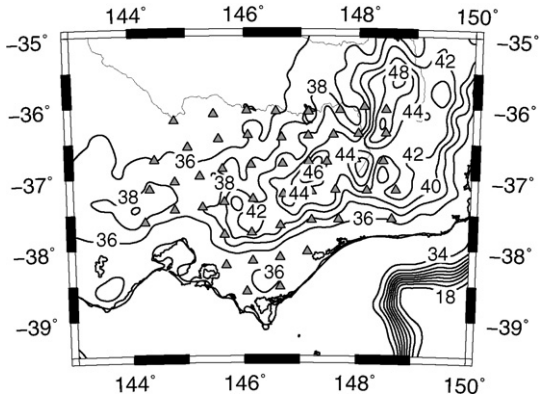

Fig. 12. Moho depth map used as *a priori* information in the tomographic inversion results shown in Fig. 13. Contour annotations are in km below sea level.

models exhibit a low-amplitude wavespeed oscillation in regions where no anomaly exists in the input model, an effect that can be attributed to the presence of the data noise. The depth slices (Fig. 11a) show little evidence of lateral distortion of structure, but all the vertical cross-sections (Fig. 11b and c) illustrate to varying degrees the vertical smearing that is typical of teleseismic tomography. Structural elongation is most pronounced beneath the southern and northern ends of the array (Fig. 11b(vi) and c(iv)), where good angular ray coverage is limited. Nevertheless, provided the general tendency to smear structure in the near vertical direction is considered at the interpretation stage, the preceding tests appear to indicate that the resolving power of the EVA dataset is sufficient to image structural variations in the upper mantle with scale lengths of the order 40–50 km.

4.3. Accounting for Moho topography

One of the challenges in applying teleseismic tomography to the EVA dataset is trying to account for the presence of the Great Dividing Range, which varies in elevation by up to 2 km across the array. If one assumes that pointwise Airy isostasy is valid, then the corresponding variations in Moho depth could be as great as 11 km (assuming an average crustal density of 2.8×10^3 kg m^{-3} and an average upper mantle density of 3.3×10^3 kg m^{-3}) or more. While it is possible for residual contributions from variable Moho topography to be represented by shallow velocity anomalies, the resolving power of the dataset is not sufficient to properly concentrate such strong perturbations (potentially as great as 1.4 km/s) in their correct locations. Instead, they will be smeared out, and may well result in significant artifacts forming in the upper mantle. The standard way of dealing with unresolved shallow structure is to include station terms in the inversion (Frederiksen et al., 1998; Graeber et al., 2002), as has been done here. However, as was noted in the previous section, the trade-off between station terms and velocity structure is difficult to resolve, with the controlling factor being the choice of regularisation as much as the data itself. The pattern of station terms shown in Fig. 8 exhibit little evidence of significant Moho topography, but for the above reasons, this is a somewhat equivocal result.

A number of studies have attempted to overcome the limitations of station terms by instead using accurate *a priori* crustal models to correct relative arrival time residuals for the presence of unresolved shallow structure (Waldhauser et al., 2002; Lippitsch et al., 2003; Martin and Ritter, 2005; Lei and Zhao, 2007). Another approach is to simultaneously invert the teleseismic relative arrival time residuals together with any available seismic data that constrains crustal structure (e.g. wide-angle refraction and reflection travel times), as was done in a recent paper by Rawlinson and Urvoy (2006). The difficulty here is that *a priori* knowledge of crustal structure beneath eastern Victoria is very limited, and no complementary data set with good crustal coverage exists. Nevertheless, the influence of Moho topography on the reconstruction of upper mantle velocity structure is examined by introducing a depth varying Moho surface to the velocity model. The surface is based on the complimentary studies of Clitheroe et al. (2000) and Collins et al. (2003), who constructed Australia-wide maps of Moho depth using receiver function and reflection/refraction profiling results. Due to the low-spatial resolution of these models, we introduce additional

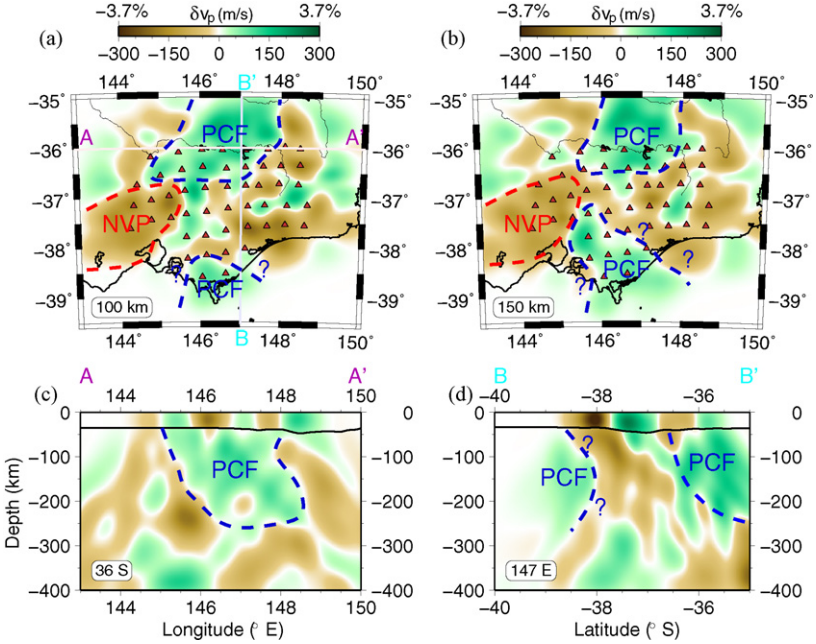

Fig. 13. A selection of slices through the solution model that contains a depth varying Moho surface with several features of interest highlighted. (a) Depth slice at 100 km; (b) depth slice at 150 km; (c) E–W cross-section at 36°S; (d) N–S cross-section at 147°E. NVP: Newer Volcanic Province; PCF: Proterozoic Continental Fragment.

detail by assuming pointwise Airy isostacy with the GTOPO30 and ETOPO2 DEMs. The resultant Moho map (Fig. 12) is defined using a grid spacing of 16 km.

The robustness of the short wavelength features of the composite model is dependent on the two basic assumptions of Airy isostasy: a lack of lithospheric strength, and an absence of lateral variations in density within the crust. However, the fact that Fig. 12 satisfies the *a priori* Moho depth information and correlates well with the pattern of Bouguer gravity anomalies in eastern Victoria (Douglas and Ferguson, 1988) at least indicates that it is consistent with available geophysical data.

Fig. 13 shows several slices through the tomographic solution model that incorporates the variable Moho topography shown in Fig. 12. As before, six iterations of a 20-dimensional subspace inversion scheme are used to satisfy the data. In this case, the RMS data misfit of the solution model is 101 ms, a slight improvement over the Moho-free model shown in Figs. 6 and 7. Both crust and upper mantle velocity are permitted to vary in the inversion, but Moho geometry remains fixed since it is not possible to resolve the trade-off between interface depth and velocity variation. The presence of the Moho surface means that there is no implicit smoothing (from the parameterisation) or explicit smoothing (from the regularisation) between crust and upper mantle velocities.

A comparison between the solution model that includes a Moho surface (Fig. 13) and the solution model that does not (Figs. 6 and 7) reveals some significant differences to depths of approximately 70 km. However, below this zone, the patterns of wavespeed variation are remarkably similar. Clearly, in this case, unresolved near surface anomalies do not manifest as artifacts deeper in the mantle; rather their effects are limited to the crust and uppermost mantle. Even if the finer detail of the Moho model we adopt here is not a good approximation to the truth, it is unlikely that the pattern of velocity anomalies will change markedly below depths of ~70 km.

5. Discussion

Previous seismic studies that image the upper mantle in the vicinity of the EVA array include the on-going continent-wide surface wave tomography project, initiated by the SKIPPY deployments between 1993–1998 (Zielhuis and van der Hilst, 1996; Debayle and Kennett, 2000; Simons et al., 2002; Fishwick et al., 2005); a teleseismic tomography study in western Victoria (Graeber et al., 2002); and a teleseismic tomography study in southern NSW (Rawlinson et al., 2006a). Comparison of the tomographic results from EVA with those of SKIPPY and its successors is not particularly enlightening, as the minimum scale length of structure resolved by the surface wave tomography is of the order of 200 km or more. In the most recent surface wave images (Fishwick et al., 2005), it is possible to identify a N–S decrease in shear wavespeed from southern NSW into eastern Victoria at 100 km depth, which is broadly consistent with our results (Fig. 6a and b). Between 200 and 300 km depth, this trend reverses, with higher shear wavespeeds beneath Victoria than NSW. While the correlation of this feature with the pattern of anomalies in Fig. 6d–f is less certain, by 300 km depth, eastern Victoria is underlain by higher wavespeeds than southern NSW.

The teleseismic tomography study of western Victoria undertaken by Graeber et al. (2002) uses data from a 40 instrument array with a similar station spacing to that of EVA. Consequently, they were able to delineate structures at a similar depth range and scale-length to this study. Resolved portions of the two solution models overlap beneath the western edge of EVA, where the agreement is generally good. The most prominent feature found by Graeber et al. (2002) in this region is a pronounced negative velocity anomaly extending to a depth of approximately 150 km, which they attribute to elevated temperatures associated with the newer volcanic province, a region of late tertiary and quaternary hot-spot related volcanism. Negative velocity anomalies beneath the south-western sector of the EVA array (Fig. 13) also lie below the NVP, and appear to confirm the findings of the previous study. However, since the resolution of the teleseismic dataset decreases rapidly below asthenospheric depths, it is unclear whether the magmatism is plume related, or simply derives from a shallow asthenospheric mantle source, as has recently been suggested by Paul et al. (2005).

To the north of EVA, distant earthquakes recorded by an array of 20 temporary stations were analysed by Rawlinson et al. (2006a) using teleseismic tomography. They found elevated wavespeeds beneath the Wagga–Omeo Complex (central sub-province of the Lachlan Orogen) in NSW that span a depth range of 80–250 km. The central sub-province represents the main concentration of Palaeozoic high-temperature low-pressure metamorphism in the Lachlan Orogen. A number of authors (Foster and Gray, 2000; Spaggiari et al., 2003; Gray and Foster, 2004) have suggested that this region evolved via eastward subduction of oceanic lithosphere beneath an island arc complex to form a high-temperature metamorphic/plutonic zone in the Late Ordovician, followed by juxtaposition of the Tabberabbera and Melbourne Zones (Fig. 1) as a consequence of double-divergent subduction. In this scenario, the elevated wavespeeds would be a signature of locally thickened or imbricated oceanic lithosphere.

An alternative model for the formation of the central subprovince (Willman et al., 2002) involves extensive strike–slip motion along the Baragwanath transform between the so-called Whitelaw and Benambra Terranes. Here, the Whitelaw Terrane represents the western subprovince, and the Benambra Terrane represents the central and eastern subprovinces. Rawlinson et al. (2006a) acknowledge the possibility that continental lithosphere of Proterozoic origin underlying the Benambra Terrane may also give rise to the elevated wavespeeds observed beneath the Wagga–Omeo Complex.

Historically, both composition (Griffin et al., 1998) and temperature (Cammarano et al., 2003) have been used to explain the differences in wavespeed observed in the mantle lithosphere. In a recent study, Faul and Jackson (2005) use laboratory measurements of shear wavespeed in melt-free polycrystalline aggregates of olivine to suggest that the variations in wavespeed observed in the continental shear wave model of Fishwick et al. (2005) can be explained by physically reasonable temperature anomalies. Thus, the older lithosphere beneath Precambrian western Australia may simply be thicker and cooler than the younger and thinner Palaeozoic lithosphere that underlies much of eastern Australia.

Although the relative importance of temperature and composition to the P and S wavespeed of the Australian lithosphere can be debated, it is apparent that Precambrian continental mantle lithosphere will exhibit higher P or S wavespeeds than its Phanerozoic counterpart. Due to the coverage of the array in NSW, Rawlinson et al. (2006a) were unable to assess the southern extent of the elevated velocity anomaly observed beneath the Wagga–Omeo Complex. In the current study, the positive wavespeed perturbations beneath the northern end of the array (Fig. 13) correlate quite closely with the tomography results from NSW, and it is clear that the anomaly does not extend very far south. This result provides more support to the contention that the central subprovince of the Lachlan Orogen is underlain by a Proterozoic continental fragment (or PCF, see Fig. 13), than the idea of a locally imbricated lithosphere resulting from E–W convergent subduction accretion. If subduction was the causal mechanism, one would expect the positive wavespeed anomaly to have a greater N–S extent; however, we do not rule out this possibility.

It is not clear that the presence of a PCF beneath northern Victoria and southern NSW (as inferred in Fig. 13) requires emplacement via continental scale strike–slip faulting without the need for a subduction–accretion system, as favoured by Willman et al. (2002). In fact, the potential for fragments or ribbons of Proterozoic continental lithosphere, detached from the eastern margin of Australia during the Neoproterozoic break-up of Rodinia, to be intermixed with the accretionary melange of the Lachlan Orogen, has been considered by a number of authors (Glen et al., 1992; Cayley et al., 2002; Betts et al., 2002; Gray and Foster, 2004; Glen, 2005). It may well be that our inferred PCF is one of a number of these fragments scattered throughout the region. For instance, the case for a so-called Selwyn Block, comprising a large fragment of Proterozoic lithosphere underlying western Tasmania and extending northward beneath the Melbourne Zone, has been argued by Cayley et al. (2002) on the basis of aeromagnetic and geologic data. In this scenario, the Selwyn Block existed as a continental fragment lying some distance off the east coast of Australia at the end of the Cambrian. Ensuing tectonic activity, dominated by east-west shortening, eventually resulted in the Selwyn Block being emplaced in its current position. From the results of this study, evidence for a Selwyn Block as envisaged by Cayley et al. (2002) appears tenuous. Certainly, the positive wavespeed anomaly observed beneath the southern end of the array at 100–150 km depth (see Fig. 13) could be construed as evidence of Proterozoic lithosphere, but it does not extend very far beneath Victoria; Cayley et al. (2002) infer from their data that Proterozoic crust underlies the entire Melbourne Zone, and may well extend beyond it. Reed (2001) has proposed that the transition between the Eastern and Western Tasmania Terranes extends northward to become the Governor fault, which separates the Tabberabbera and Melbourne Zones (Fig. 1). Our results show little evidence for such a feature at upper mantle depths (Fig. 13), but it should be noted that the transition observed in Tasmania by Rawlinson and Urvoy (2006) was restricted to the crust.

Most plate tectonic models for the development of the Lachlan Orogen agree that it involved a long-lived subduction zone outboard of either an intraplate backarc setting or a marginal ocean setting (Gray and Foster, 2004). Over the last decade, models involving multiple E–W convergent subduction systems in a marginal ocean setting have become popular (Gray et al., 1997; Foster and Gray, 2000; Fergusson, 2003; Spaggiari et al., 2004), although there is still considerable debate as to the number and configuration of the subduction centres. The ability of the teleseismic tomography images obtained here to address this issue is limited, because unlike active subduction zones, it is not clear what wavespeed signature might arise from an ancient subduction system frozen into the lithosphere. Given the effects of subsequent deformation and chemical alteration over a 350 Ma period, there may be no significant thermal or compositional anomaly remaining. It is possible that some of the steeply dipping high-velocity structures observed beneath the crust (e.g. Fig. 7a(iii)) may be evidence of remnant subduction, as was inferred by Rawlinson et al. (2006b) in Tasmania, but the case here is not compelling.

6. Conclusions

In this study, teleseismic P-wave tomography has been used to illuminate the upper mantle structure beneath the western and central subprovinces of the Lachlan Orogen in southeast Australia. The potential for poorly resolved heterogeneous crustal structure to manifest as prominent artifacts in mantle structure was investigated by including a strongly varying Moho surface in the inversion model, which reflects the presence of significant surface topography in eastern Victoria. Results from these tests indicate that uncertainty in *a priori* crustal information is unlikely to influence the recovery of mantle structure below about 70 km depth. The lack of a predominant orientation to the P-wavespeed anomalies in the final solution model, and evidence for the presence of a large fragment of Proterozoic continental lithosphere beneath the central subprovince, implies that a purely E–W convergent subduction accretion model for the formation of the Lachlan Orogen is not supported by these results. However, given the passage of time since the cessation of subduction in the Devonian, a lack of clear seismic evidence for remnant or fossil slabs in the upper mantle could be explained by subsequent alteration, deformation or thermal affects. In the latter case, negative wavespeed anomalies beneath the southwest sector of the array can be attributed to elevated mantle temperatures associated with upwelling magmatism beneath the Late Cenozoic Newer Volcanic Province.

Wavespeed anomalies in the upper mantle reconstructed from the EVA passive dataset appear to complement teleseismic tomography results obtained from neighbouring seismic arrays in western Victoria and southern NSW. In particular, evidence for an upper mantle source for the NVP and a Proterozoic continental fragment embedded beneath the Wagga–Omeo Complex can be found in the LF98 and SEAL tomographic models. Combining the three independent solutions into a unified map of upper mantle structure is not straightforward, however, due to edge effects which intensify smearing outboard of the array boundaries, and the use of relative arrival time residuals to constrain structure. Instead, it would be far better to combine all data in a single inversion, with some calibration of relative arrival time residual information from the separate arrays in order to minimise the loss of long wavelength features. However, this is beyond the scope of the current study, and instead will be the subject of future research.

Acknowledgments

The authors would like to thank Tony Percival, Armando Arcidiaco, Stewart Fishwick, Anya Reading and Marine Urvoy for their assistance with the deployment and servicing of the EVA seismic array. ANSIR, the Australian National Research Facility for Earth Sounding, is thanked for providing the seismic equipment used in this study. The many private landowners and organisations, including the Victorian Department of Sustainability and Environment, and the NSW National Parks and Wildlife Service, are gratefully acknowledged for freely granting us permission to install seismic stations on their land. George Helffrich and Ian Bastow are thanked for their constructive comments on the original version of this paper. This work was supported by Australian Research Council Discovery Project DP0556282.

Software availability: The adaptive stacking software package for optimum trace alignment is available at http://rses.anu.edu.au/seismology/astack, along with detailed instructions and examples. The FMTOMO package for tomographic inversion of travel time data (e.g. teleseismic, local earthquake, refraction, wide-angle reflection) for three-dimensional velocity structure, interface geometry and source location is available at http://rses.anu.edu.au/∼nick/fmtomo.html, and includes a detailed instruction manual and examples.

References

Achauer, U., 1994. New ideas on the Kenya rift based on the inversion of the combined dataset of the 1985 and 1989/90 seismic tomography experiments. Tectonophysics 236, 305–329.

Aki, K., Christoffersson, A., Husebye, E.S., 1977. Determination of the three-dimensional seismic structure of the lithosphere. J. Geophys. Res. 82, 277–296.

Bartels, R.H., Beatty, J.C., Barsky, B.A., 1987. An Introduction to Splines for Use in Computer Graphics and Geometric Modelling. Morgan Kaufmann, Los Altos.

Betts, P.G., Giles, D., Lister, G.S., Frick, L., 2002. Evolution of the Australian lithosphere. Aust. J. Earth Sci. 49, 661–695.
Bulant, P., 1996. Two-point ray tracing in 3-D. Pure Appl. Geophys. 148, 421–447.
Cammarano, F., Goes, S., Vacher, P., Giardini, D., 2003. Inferring upper-mantle temperatures from seismic velocities. Phys. Earth Planet. Inter. 138, 197–222.
Cayley, R., Taylor, D.H., VandenBerg, A.H.M., Moore, D.H., 2002. Proterozoic–Early Palaeozoic rocks and the Tyennan Orogeny in central Victoria: the Selwyn Block and its tectonic implications. Aust. J. Earth Sci. 49, 225–254.
Clitheroe, G., Gudmundsson, O., Kennett, B.L.N., 2000. The crustal thickness of Australia. J. Geophys. Res. 105, 13697–13713.
Collins, C.D.N., 1991. The nature of the crust-mantle boundary under Australia from seismic evidence. In: Drummond, B. (Ed.), The Australian Lithosphere. Vol. 17 of Special Publication. Geological Society of Australia, pp. 67–80.
Collins, C.D.N., Drummond, B.J., Nicoll, M.G., 2003. Crustal thickness patterns in the Australian continent. In: Hillis, R.R., Müller, R.D. (Eds.), Evolution and Dynamics of the Australian Plate. Vol. 22 of Special Publication. Geological Society of Australia, pp. 121–128.
de Kool, M., Rawlinson, N., Sambridge, M., 2006. A practical grid based method for tracking multiple refraction and reflection phases in 3D heterogeneous media. Geophys. J. Int. 167, 253–270.
Debayle, E., Kennett, B.L.N., 2000. The Australian continental upper mantle: structure and deformation inferred from surface waves. J. Geophys. Res. 105, 25423–25450.
Debayle, E., Kennett, B.L.N., 2003. Surface wave studies of the Australian region. In: Hillis, R.R., Müller, R.D. (Eds.), The Evolution and Dynamics of the Australian Plate. Special Publication. Geological Society of Australia and America, pp. 25–40.
Direen, N.G., Crawford, A.J., 2003. The Tasman Line: where is it, what is it, and is it Australia's Rodinian breakup boundary? Aust. J. Earth Sci. 50, 491–502.
Douglas, J.G., Ferguson, J.A., 1988. Geology of Victoria. Geological Society of Australia, Melbourne.
Evans, J.R., Achauer, U., 1993. Teleseismic tomography using the ach method: theory and application to continental scale studies. In: Iyer, H.M., Hirahara, K. (Eds.), Seismic Tomography: Theory and Practice. Chapman & Hall, London, pp. 319–360.
Faul, U.H., Jackson, I., 2005. The seismological signature of temperature and grain size variations in the upper mantle. Earth Planet. Sci. Lett. 234, 119–134.
Fergusson, C.L., 2003. Ordovician-Silurian accretion tectonics of the Lachlan Fold Belt, southeastern Australia. Aust. J. Earth Sci. 50, 475–490.
Fishwick, S., Kennett, B.L.N., Reading, A.M., 2005. Contrasts in lithospheric structure within the Australian craton—insights from surface wave tomography. Earth Planet. Sci. Lett. 231, 163–176.
Foster, D.A., Gray, D.R., 2000. Evolution and structure of the Lachlan Fold Belt (Orogen) of eastern Australia. Ann. Rev. Earth Planet. Sci. 28, 47–80.
Frederiksen, A.W., Bostock, M.G., VanDecar, J.C., Cassidy, J.F., 1998. Seismic structure of the upper mantle beneath the northern Canadian Cordillera from teleseismic travel-time inversion. Tectonophysics 294, 43–55.
Glahn, A., Granet, M., 1993. Southern Rhine Graben: small-wavelength tomographic study and implications for the dynamic evolution of the graben. Geophys. J. Int. 113, 399–418.
Glen, R.A., 2005. The Tasmanides of eastern Australia. In: Vaughan, A.P.M., Leat, P.T., Pankhurst, R.J. (Eds.), Terrane processes at the margins of Gondwana. Geological Society, London, pp. 23–96.
Glen, R.A., Scheibner, E., Vandenberg, A.H.M., 1992. Paleozoic intraplate escape tectonics in Gondwanaland and major strike–slip duplication in the Lachlan Orogen of south-eastern Australia. Geology 20, 795–798.
Graeber, F.M., Asch, G., 1999. Three-dimensional models of *P* wave velocity and *P*-to-*S* velocity ratio in the southern central Andes by simultaneous inversion of local earthquake data. J. Geophys. Res. 104, 20237–20256.
Graeber, F.M., Houseman, G.A., Greenhalgh, S.A., 2002. Regional teleseismic tomography of the western Lachlan Orogen and the Newer Volcanic Province, southeast Australia. Geophys. J. Int. 149, 249–266.
Gray, D.R., Foster, D.A., 2004. Tectonic evolution of the Lachlan Orogen, southeast Australia: historical review, data synthesis and modern perspectives. Aust. J. Earth Sci. 51, 773–817.
Gray, D.R., Foster, D.A., Butcher, M., 1997. Recognition and definition of orogenic events in the Lachlan Fold Belt. Aust. J. Earth Sci. 44, 489–581.
Griffin, W.L., O'Reilly, S.Y., Ryan, C.G., Gaul, O., Ionov, D.A., 1998. Secular variation in the composition of subcontinental lithospheric mantle: geophysical and geodynamic implications. In: Braun, J., Dooley, J., Goleby, B., van der Hilst, R., Kllotwijk, C. (Eds.), In: Structure and evolution of the Australian continent, Vol. 26. American Geophysical Union Geodynamic Series, pp. 1–26.
Hearn, T.M., Clayton, R.W., 1986. Lateral velocity variations in southern California. I. Results for the upper crust from *Pg* waves. Bull. Seism. Soc. Am. 76, 495–509.
Humphreys, E.D., Clayton, R.W., 1990. Tomographic image of the Southern California Mantle. J. Geophys. Res. 95, 19725–19746.
Julian, B.R., Gubbins, D., 1977. Three-dimensional seismic ray tracing. J. Geophys. 43, 95–113.
Kennett, B.L.N., Engdahl, E.R., Buland, R., 1995. Constraints on seismic velocities in the earth from travel times. Geophys. J. Int. 122, 108–124.
Kennett, B.L.N., Fishwick, S., Reading, A.M., Rawlinson, N., 2004. Contrasts in mantle structure beneath Australia: relation to Tasman Lines? Aust. J. Earth Sci. 51, 563–569.
Kennett, B.L.N., Sambridge, M.S., Williamson, P.R., 1988. Subspace methods for large scale inverse problems involving multiple parameter classes. Geophys. J. 94, 237–247.
Lei, J., Zhao, D., 2007. Teleseismic P-wave tomography and the upper mantle structure of the central Tien Shan orogenic belt. Phys. Earth Planet. Inter. 162, 165–185.
Lippitsch, R., Kissling, E., Ansorge, J., 2003. Upper mantle structure beneath the Alpine orogen from high-resolution teleseismic tomography. J. Geophys. Res. 108, 2376.
Martin, M., Ritter, J.R.R., the CALIXTO working group, 2005. High-resolution teleseismic body-wave tomography beneath SE Romania. I. Implications for the three-dimensional versus one-dimensional crustal correction strategies with a new crustal velocity model. Geophys. J. Int. 162, 448–460.
Meert, J.G., 2001. Growing Gondwana and rethinking Rodinia: a paleomagnetic perspective. Gondwana Res. 4, 279–288.
Oncescu, M.C., Burlacu, V., Anghel, M., Smalbergher, V., 1984. Three-dimensional *P*-wave velocity image under the Carpathian Arc. Tectonophysics 106, 305–319.
Paul, B., Hergt, J.M., Woodhead, J.D., 2005. Mantle heterogeneity beneath the Cenozoic volcanic provinces of central Victoria inferred from trace-element and Sr, Nd, Pb and Hf isotope data. Aust. J. Earth Sci. 52, 243–260.
Popovici, A.M., Sethian, J.A., 2002. 3-D imaging using higher order fast marching traveltimes. Geophysics 67, 604–609.
Prothero, W.A., Taylor, W.J., Eickemeyer, J.A., 1988. A fast, two-point, three-dimensional raytracing algorithm using a simple step search method. Bull. Seism. Soc. Am. 78, 1190–1198.
Rawlinson, N., Houseman, G.A., Collins, C.D.N., 2001. Inversion of seismic refraction and wide-angle reflection traveltimes for 3-D layered crustal structure. Geophys. J. Int. 145, 381–401.
Rawlinson, N., Kennett, B.L.N., 2004. Rapid estimation of relative and absolute delay times across a network by adaptive stacking. Geophys. J. Int. 157, 332–340.
Rawlinson, N., Kennett, B.L.N., Heintz, M., 2006a. Insights into the structure of the upper mantle beneath the Murray Basin from 3D teleseismic tomography. Aust. J. Earth Sci. 53, 595–604.
Rawlinson, N., Reading, A.M., Kennett, B.L.N., 2006b. Lithospheric structure of Tasmania from a novel form of teleseismic tomography. J. Geophys. Res. 111.
Rawlinson, N., Sambridge, M., 2003. Seismic traveltime tomography of the crust and lithosphere. Adv. Geophys. 46, 81–198.
Rawlinson, N., Sambridge, M., 2004a. Multiple reflection and transmission phases in complex layered media using a multistage fast marching method. Geophysics 69, 1338–1350.
Rawlinson, N., Sambridge, M., 2004b. Wavefront evolution in strongly heterogeneous layered media using the fast marching method. Geophys. J. Int. 156, 631–647.
Rawlinson, N., Sambridge, M., 2005. The fast marching method: an effective tool for tomographic imaging and tracking multiple phases in complex layered media. Explor. Geophys. 36, 341–350.
Rawlinson, N., Urvoy, M., 2006. Simultaneous inversion of active and passive source datasets for 3-D seismic structure with application to Tasmania. Geophys. Res. Lett. 33.
Reed, A.R., 2001. Pre-Tabberabberan deformation in eastern Tasmania: a southern extension of the Benambran Orogeny. Aust. J. Earth Sci. 48, 785–796.
Sambridge, M.S., 1990. Non-linear arrival time inversion: constraining velocity anomalies by seeking smooth models in 3-D. Geophys. J. Int. 102, 653–677.
Sethian, J.A., 1996. A fast marching level set method for monotonically advancing fronts. Proc. Natl. Acad. Sci. 93, 1591–1595.
Sethian, J.A., 2001. Evolution, implementation, and application of level set and fast marching methods for advancing fronts. J. Comp. Phys. 169, 503–555.
Simons, F.J., van der Hilst, R.D., Montagner, J.-P., Zielhuis, A., 2002. Multimode Rayleigh wave inversion for heterogeneity and azimuthal anisotropy of the Australian upper mantle. Geophys. J. Int. 151, 738–754.
Spaggiari, C.V., Gray, D.R., Foster, D.A., 2004. Lachlan Orogen subduction–accretion systematics revisited. Aust. J. Earth Sci. 51, 549–553.
Spaggiari, C.V., Gray, D.R., Foster, D.A., McKnight, S., 2003. Evolution of the boundary between the western and central Lachlan Orogen: implications for Tasmanide tectonics. Aust. J. Earth Sci. 50, 725–749.
Steck, L.K., Thurber, C.H., Fehler, M., Lutter, W.J., Roberts, P.M., Baldridge, W.S., Stafford, D.G., Sessions, R., 1998. Crust and upper mantle *P* wave velocity structure beneath Valles caldera, New Mexico: results from the Jemez teleseismic tomography experiment. J. Geophys. Res. 103, 24301–24320.
Taylor, D.H., Cayley, R.A., 2000. Character and kinematics of faults within the turbidite-dominated Lachlan Orogen: implications for tectonic evolution of eastern Australia: Discussion. J. Struct. Geol. 22, 523–528.
Um, J., Thurber, C., 1987. A fast algorithm for two-point seismic ray tracing. Bull. Seism. Soc. Am. 77, 972–986.
VandenBerg, A.H.M., 1999. Timing of orogenic events in the Lachlan Orogen. Aust. J. Earth Sci. 46, 691–701.
Waldhauser, F., Lippitsch, R., Kissling, E., Ansorge, J., 2002. High-resolution teleseismic tomography of upper-mantle structure using an a priori three-dimensional crustal model. Geophys. J. Int. 150, 403–414.
Williams, E., 1989. Summary and synthesis. In: Burrett, C.F., Martin, E.L. (Eds.), Geology and Mineral Resources of Tasmania. Vol. 15 of Special Publication. Geological Society of Australia, pp. 468–499.
Williamson, P.R., 1990. Tomographic inversion in reflection seismology. Geophys. J. Int. 100, 255–274.
Willman, C.E., VandenBerg, A.H.M., Morand, V.J., 2002. Evolution of the southeastern Lachlan Fold Belt in Victoria. Aust. J. Earth Sci. 49, 271–289.
Zielhuis, A., van der Hilst, R.D., 1996. Upper-mantle shear velocity beneath eastern Australia from inversion of waveforms from SKIPPY portable arrays. Geophys. J. Int. 127, 1–16.